

# Using gravity gradients to estimate fault parameters in the Wichita Uplift region

Sibel Uzun,<sup>1</sup> Kamil Erkan<sup>2</sup> and Christopher Jekeli<sup>3</sup>

<sup>1</sup>Division of Geomatics Engineering, Ondokuz Mayıs University, 55200, Turkey. E-mail: [uzun.1@buckeyemail.osu.edu](mailto:uzun.1@buckeyemail.osu.edu)

<sup>2</sup>Department of Environmental Engineering, Marmara University, Göztepe, Istanbul, 34722, Turkey

<sup>3</sup>Division of Geodetic Science, School of Earth Sciences, Ohio State University, Columbus, OH, 43210, USA

Accepted 2020 May 26. Received 2020 May 26; in original form 2019 June 15

## SUMMARY

The geological setting of southwestern Oklahoma and northeastern Texas is an ideal example of an aulacogen, the result of the tectonic evolution of a failed rift of the North American continent during the Palaeozoic era (540–360 Ma). The Wichita Province forms the uplifted basement portion of this Southern Oklahoma Aulacogen (SOA). The major fault zones to its north and south are clearly evident in gravity gradient maps produced by the recently constructed Earth Gravitational Model 2008 (EGM2008). Fault parameters, such as the dip angle, location and density contrasts have been estimated from profiles of seismic data and local gravimetry in the 1990s. On the other hand, gravitational gradients that are derived from EGM2008 and then combined to form the differential field curvature are particularly indicative of linear structures such as dip-slip faults. They are used here exclusively, that is, without additional geophysical constraints, in an optimal, least-squares estimation based on the Monte Carlo technique of simulated annealing to determine dip angle and location parameters of the major faults that border the Wichita Uplift region. Results show that these faults have small dip angles, in basic agreement with the low-angle faults inferred from seismic studies. The EGM2008 gradients also appear in some cases to provide an improved map of the major faults in the region, thus offering a strong constraint on their location.

**Key words:** Inverse theory; Numerical modelling; Dynamics: gravity and tectonics.

## 1 INTRODUCTION

The region of southwestern Oklahoma and northeastern Texas is distinctive in terms of its geology and tectonics. Geologically, it is bounded by major fault zones to the north and south, beyond which are deep and extensive basins, the Hollis–ardeman Basin in the south and the Anadarko Basin in the north. The latter is the deepest continental basin of North America and bears large amounts of hydrocarbon deposits (Perry 1989). From the perspective of plate tectonics, it is an ideal example of an ‘aulacogen’, or the result of a failed rift of the North American continent (Hoffman *et al.* 1974). The rifting, dating to the early Palaeozoic (~540 Ma), was followed by subsidence of the region during the middle Palaeozoic (~440 Ma) and a subsequent uplift due to compression in the late Palaeozoic (~300 Ma) (Keller and Baldridge 1995). The Wichita Province forms the uplifted basement portion of this Southern Oklahoma Aulacogen (SOA, Fig. 1a). The eastern boundary of the region is more transitional than the faulted northern and southern boundaries, with thickening of the sedimentary layer toward the Ardmore Basin. In the west, the uplifted region extends to the Texas panhandle, and changes its name to the Amarillo uplift. The Wichita section of the uplift shows the most profound structural and tectonic features while

these features die away in the Amarillo side toward the west. Various investigators (Ham *et al.* 1964; Wickham 1978; Brewer *et al.* 1983; Coffman *et al.* 1986; Chang *et al.* 1989; Hamilton 1989; Keller and Stephenson 2007) have generated 2-D structural models based on gravity and seismic data across the strike of the principal faults in the Wichita Uplift region.

The first extensive study on the geological units and structural features of this region was made by Ham *et al.* (1964), which includes information on ages, chemical compositions and thicknesses of the rock units based on data from boreholes (obtained in conjunction with extensive petroleum exploration), as well as snapshots of structural cross-sections and the inferred tectonic history of the region. Ham *et al.* (1964) characterize the faults as high-angle faults to the north and south of the Wichita Uplift region in their study. The petrologic properties of exposed igneous rocks in the region have also contributed to the knowledge of the inferred aulacogen (Gilbert 1983). A detailed seismic profiling of the internal structures of the SOA, conducted by the Consortium for Continental Reflection Profiling (COCORP), was first published in the early 1980s (Brewer 1982). This was followed by a second seismic reflection/refraction experiment in the same area by the Universities of Texas, Dallas and El Paso, in the mid-1980s (Chang *et al.* 1989). These seismic

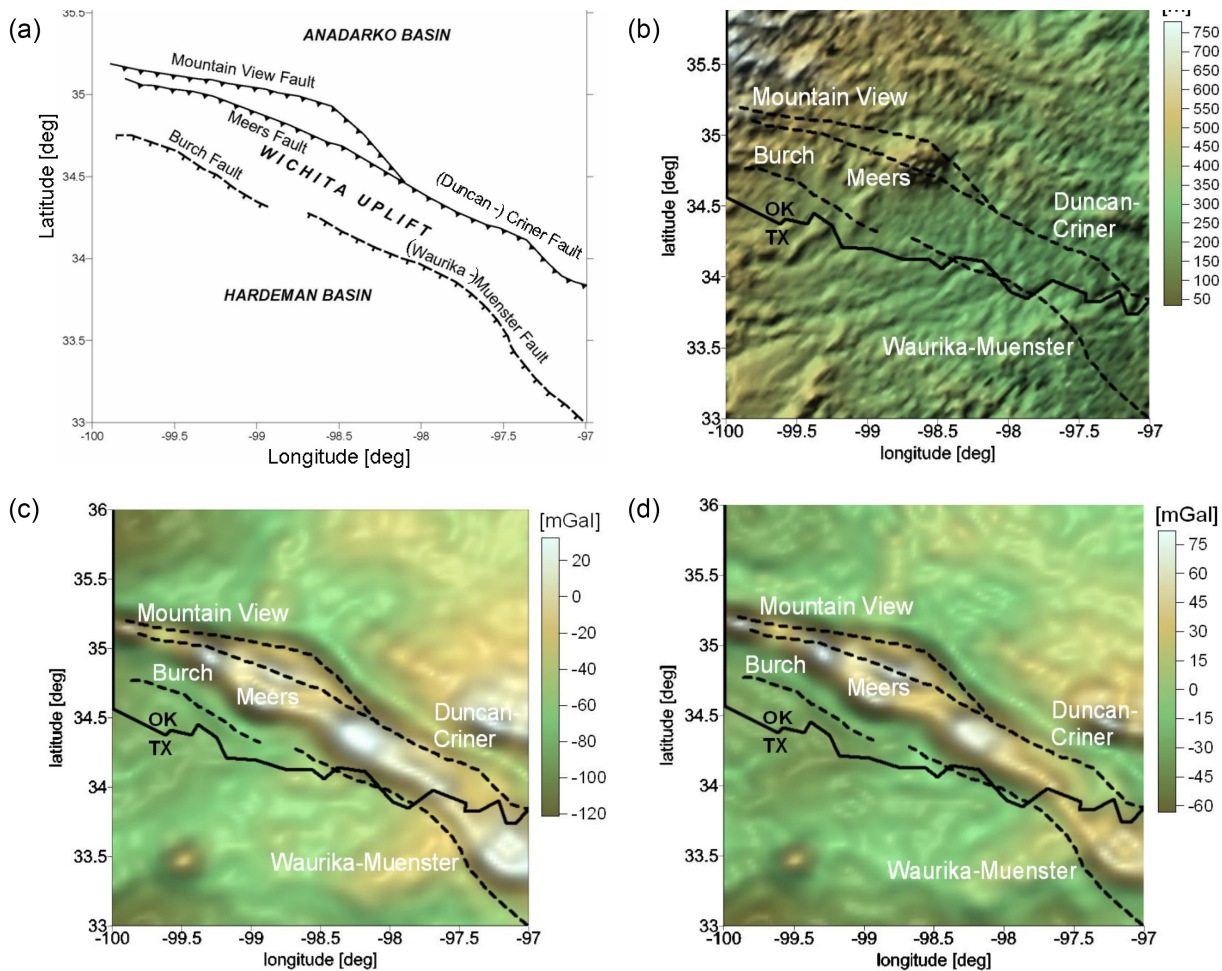


**Figure 1.** (a) Map of the faults in the Wichita Uplift region in Southern Oklahoma from geological studies, adapted from Keller and Baldrige (1995). (b) Topographic map from 9-arcsec data generated by SRTM. (c) The Bouguer gravity anomaly derived from the EGM2008 and DTM2006 models (Pavlis *et al.* 2012). (d) The free-air gravity anomaly,  $\Delta g$ , derived from EGM2008. All gravity quantities are defined in Appendix A. The indicated fault lines in (b)–(d) are transcribed from (a).

data indicated extensive low-angle faulting associated with the rift, where, for example, the northeasterly thrust of the Wichita mountains over the Anadarko Basin occurred along faults that dip to the southwest.

Surface gravity measurements have been obtained at different times by different agencies. One of the more recent compilations of gravity data was made by Robbins and Keller (1992) of more than 11 000 points over the SOA and surrounding areas. Their generated residual isostatic anomaly map clearly identifies the aulacogen with an elongated southeast-to-northwest trending positive anomaly (80 mGal), which could not be explained by any changes in crustal thickness and is due entirely to density variations within the upper crust. The sharp drops in the gravity field on both sides of the uplift indicate the existence of large structural offsets. The gravity anomaly here is the second largest in the North American continent after the one associated with the mid-continent rift.

Analogous to the seismic interpretations, various 2-D structural models were generated from the gravity data across the strike of the anomaly. Earlier studies pointed to a large mafic intrusion under the Wichita uplift to explain the observed gravity anomaly (Pruett 1974; Papesh 1983). A more detailed structural model (Coffman *et al.* 1986) that included petrologic and geological constraints posited

two mafic intrusions, a shallow one down to 3 km and a deeper one at 15–20 km with slightly higher density. An alternative structural model assumes a single continuous mafic intrusion from the surface down to 20 km depth (Hamilton 1989; Robbins and Keller 1992; Keller and Baldrige 1995), but with varying density of the mafic body from 2.64 to 2.96  $\text{gm cm}^{-3}$  as the depth increases. Wickham (1978) also considered a single mafic intrusion near the centre of the aulacogen having a density of 3.14  $\text{gm cm}^{-3}$  with a root to match the observed gravity. Using the seismic data as constraints in an inversion of the recent gravity data, Keller and Baldrige (1995) produced a structural profile of the Wichita Uplift region. They modelled the faults as a mix of high- and low-angle faults in agreement with the fault models constructed by Wickham (1978), Coffman *et al.* (1986) and Hamilton (1989). A review of this and previous studies that contributed to an understanding of the structural evolution of the SOA may be found in Keller and Stephenson (2007), and references therein.

Fig. 1 also shows the topography of this region obtained from the SRTM (Shuttle Radar Topography Mission, Farr *et al.* 2007), as well as Bouguer and free-air gravity anomaly maps based on the high-resolution EGM2008 model (Earth Gravitational Model 2008, see below; Pavlis *et al.* 2012), which roughly reflect the regional

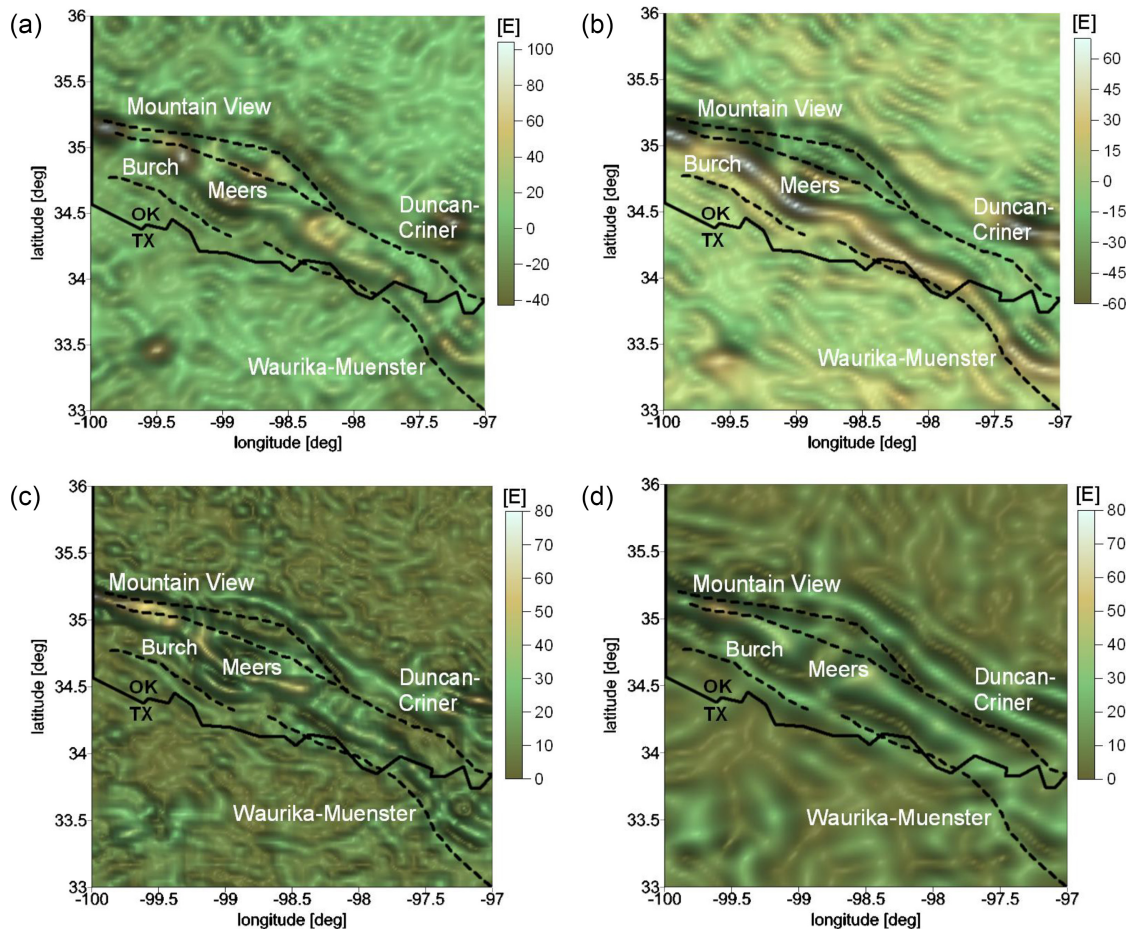


**Figure 2.** Gravitational gradient signatures of the fault zones based on the EGM2008 model. (a) The vertical gradient of gravity,  $\Gamma_{3,3}$ . (b) The cross-strike gradient of gravity,  $\Gamma_{u,w}$  (azimuth of nominal direction orthogonal to the strike =  $32.91^\circ$ ). (c) Differential-curvature gradient,  $\Gamma_C$ , computed up to maximum harmonic degree,  $n_{\max} = 2160$ ; and (d) up to  $n_{\max} = 1080$ . All gradient quantities are defined in Appendix A. The indicated fault lines in (a)–(d) are transcribed from Fig. 1(a).

faulting. It is the purpose of this paper to show that gravity gradients (Section 2) in this area provide a more visually detailed map of the faults associated with the SOA, and that inversion of these data using 2-D models leads to reasonable estimates of essential geometric parameters of the major faults, such as location and dip angle. Depth and density parameters, in principle, could be included in the estimation algorithm, but, as it is well known, the inversion of gravity data to obtain such estimates generally is not robust. Indeed, values of these parameters are fixed to determinations found previously by seismic and other *in situ* measurements. Our method of inversion (Section 3) is a probabilistically directed Monte Carlo approach called simulated annealing that operates on the nonlinear forward model of the gradients to obtain optimal, self-consistent estimates of location and dip angle.

## 2 GRAVITY GRADIENT MODEL

The latest Earth Gravitational Model, EGM2008, was constructed to high resolution from a combination of satellite orbital analyses, terrestrial, airborne and ship-borne gravimetry, and satellite altimetry data (over the oceans, Pavlis *et al.* 2012). It is a spherical harmonic series expansion complete to degree 2190 and order 2160 and thus possesses spatial resolution (half-wavelength) of about 5', or about 9 km, at the equator. The short-wavelength

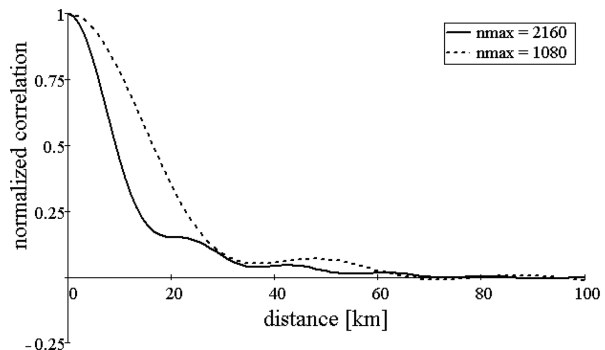


**Figure 3.** Autocorrelation functions for the vertical gradient of gravity,  $\Gamma_{3,3}$  (Appendix A), according to the EGM2008 model truncated at  $n_{\max} = 1080$  (dashed line) and  $n_{\max} = 2160$  (solid line).

gravity data in the Wichita Uplift region that contributed to this model comprise 5' mean gravity anomaly values supplied by the U.S. National Geospatial-Intelligence Agency (NGA). The original raw point data have a higher resolution (see e.g. Robbins and Keller 1992), hence, no additional mass–density contribution was necessary (as in some other parts of the world) to achieve the resolution of the model (Pavlis *et al.* 2012). The EGM2008 model thus offers an accurate and easy method to calculate gravity and gravitational

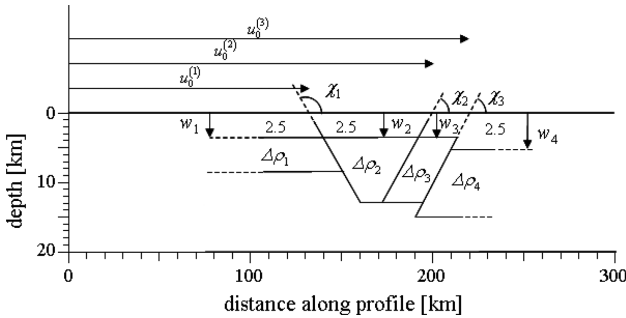


**Figure 4.** Forward model of the fault structure for the Wichita Uplift region consisting of three fault planes at angles,  $\chi_j$ , relative to the horizontal, at locations,  $u_0^{(j)}$ , relative to the endpoint of a particular profile,  $j = 1, 2, 3$ , and dividing the substructure into four displaced layers at depths,  $w_k$  (upper bounds), with density contrasts,  $\Delta\rho_k$ , relative to  $2.5 \text{ gm cm}^{-3} = 2500 \text{ kg m}^{-3}$ ,  $k = 1, \dots, 4$ . The lower depth boundaries and the density contrasts are fixed to values given in Table 1.

gradients in this region up to its defined resolution. By calculating the gravitational gradients, and specifically the magnitude of the differential curvature of the field (Appendix A), the subsurface structure appears much better delineated (Fig. 2). Although the vertical gradient of gravity (Fig. 2a) yields an improved outline of the faults, the differential-curvature gradient (Figs 2c and d) offers the most detailed visualization. Indeed, the fault lines identified by geological studies, as shown in Fig. 1(a), correspond roughly with the lineaments implied by the gravity gradients, although the latter appear to displace some of the faults from their surface locations. In part this may be due to the fact that a plane fault can give rise to two differential-curvature highs, depending on the dip angle and depths of the density contrasts (Appendix B). However, our estimation results also indicate a distinct discrepancy between some fault locations as indicated in Fig. 1(a) and as derived from the EGM2008 model. Fig. 2(b) shows that the cross-strike gradient of gravity (Appendix A) also provides a visually detailed map of the faults, but unlike for the differential-curvature gradient, construction of this map requires knowledge of the strike angle. Finally, it is noted that none of the calculated gradients appear correlated with the topography (Fig. 1b), thus confirming that they reflect deeper structure rather than near-surface topographic effects.

The differential-curvature maps in Fig. 2 are shown for two resolutions of the EGM2008 model, maximum degree and order 2160, and 1080. The east–west resolution of the  $n_{\max} = 2160$  model in this region is about 7.6 km; for the  $n_{\max} = 1080$  model it is about 15.3 km. The faults and subsurface geology modelled, for example, by Keller and Stephenson (2007) show density contrasts primarily in the upper 7–10 km of the crust. A general empirical relation between the depth of an anomalous density layer and the correlation distance (the  $1/e$  point of the autocorrelation function) of the surface field was postulated by Jordan (1978), specifically that the least depth of a density contrast represented by the field model corresponds approximately to its correlation distance. Fig. 3 shows that the correlation distance for the vertical gradient of gravity according to the EGM2008 gradient model with  $n_{\max} = 2160$  is about 11 km, while it is about 20 km for the  $n_{\max} = 1080$  model. Applying Jordan’s empirical relationship, the latter model likely is not indicative of density contrasts in the top 10 km of crust. For example, the Meers fault seems evident in the  $n_{\max} = 2160$  model but not in the  $n_{\max} = 1080$  model. On the other hand, from seismic data, Brewer *et al.* (1983) predict extensions of some major faults to depths of several 10s of km, which is reinterpreted as

such also by Gay (2014). Thus, the  $n_{\max} = 1080$  model can be used to infer fault characteristics of deep faults. We consider both spherical harmonic expansions as appropriate ‘observational’ data if they conform reasonably to signatures consistent with a plane fault model.

Estimating the fault parameters from the differential curvature of the field requires a corresponding forward model for the gravitational gradients. For each major fault we assume a single plane infinitely extended in one horizontal dimension at a strike orientation implied by the generally elongated features of the SOA. Appendix B gives the mathematical model, derived by Uzun (2013), and generalized here for multiple layers that have slipped along the fault plane, as illustrated in Fig. B.1. The major faults shown in Fig. 1(a), Burch, Waurika-Muenster, Meers, Mountain View and Duncan-Criner, are modelled locally as planes with corresponding parameters defined in Fig. 4. Introducing a local  $u, v, w$  coordinate system, with  $u$  orthogonal to the strike and  $w$  along the vertical, positive upward, the only non-zero gravitational gradients for this model are  $\Gamma_{u,u}$ ,  $\Gamma_{u,w}$  and  $\Gamma_{w,w}$ , where, for example,  $\Gamma_{w,w} = \partial^2 V / (\partial w)^2$ , and  $V$  is the gravitational potential. Any derivative of the gravitational potential generated by the model in the  $v$ -direction (parallel to the strike) vanishes. Laplace’s equation (for gradients in free space) then also gives  $\Gamma_{u,u} = -\Gamma_{w,w}$ . The gravitational gradient that represents the magnitude of the ‘differential-curvature’ of the potential field (Heiland 1940), given by eq. (A9), for the model is thus,

$$\Gamma_C = \sqrt{(\Gamma_{v,v} - \Gamma_{u,u})^2 + (2\Gamma_{u,v})^2} = |\Gamma_{w,w}|, \quad (1)$$

which is also equal to  $|\Gamma_{3,3}|$  in the local northeast-down frame (Appendix A).

The forward model of the gradients to be fitted to the observational data is based generally on the geological model of Keller and Baldridge (1995) and is shown schematically in Fig. 4 for a profile orthogonally crossing multiple plane faults. The surface locations, the dip angles and (possibly) the depths of the density contrasts are parameters of the forward model; while the density contrast values are inferred from recent values summarized by Keller and Stephenson (2007) who determined them by gravity and seismic modelling over a profile orthogonal to the strike of the faults. According to this density model, the density contrasts between local layers  $k-1$  and  $k$  can be computed as  $\Delta\rho_k = \rho_k - 2500 \text{ kg m}^{-3}$ ,  $k = 1, 2, \dots$ . The reference density of  $2500 \text{ kg m}^{-3}$  is fictitious and may be assumed as the density of the top most layer.

The obvious linear features in Figs 2(c) and (d) are somewhat deceptive because they do not clearly show the along-strike magnitudes. Fig. 5 offers another perspective of the same maps, in this case illustrating the changes in magnitude along each linear feature. Neither one shows constant magnitude along any of the linear features, but the  $n_{\max} = 1080$  model appears even less consistent, particularly along the central high between the Mountain View and Burch faults. Because the forward model of the differential curvature for a fault assumes constant magnitude along the strike, we choose cross-strike profiles, as indicated in Fig. 6, to estimate the fault parameters where the magnitude is reasonably constant in the vicinity of the profile.

### 3 PARAMETER ESTIMATION

Although the optimal estimation of parameters could be accomplished using traditional non-linear least-squares (e.g. Teunissen 1990), we use a probabilistically directed Monte Carlo approach, called simulated annealing. This method inverts the data without

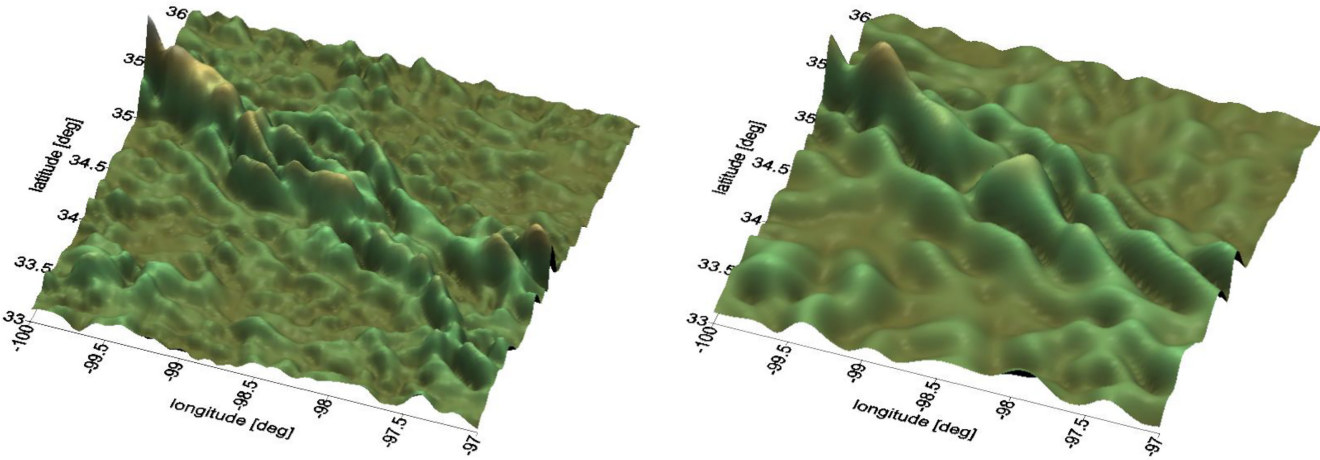


**Figure 5.** Differential curvature of the gravitational field, modelled by EGM2008 (left:  $n_{\max} = 2160$  and right:  $n_{\max} = 1080$ ) as in Figs 2(c) and (d) (same colour scale), but shown from a different perspective. Note the along-strike variations in magnitudes, which may be due to local changes at depths of high density anomalies.

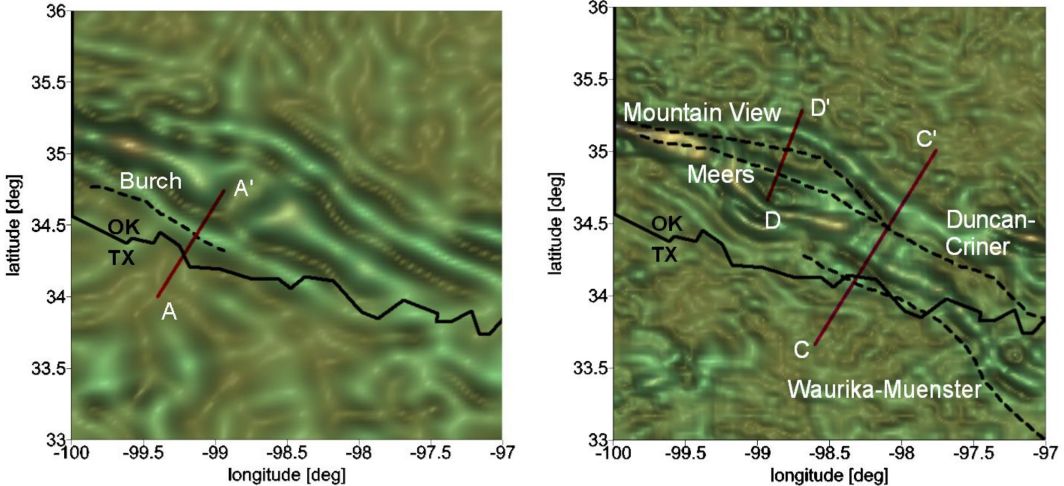


**Figure 6.** Profiles  $AA'$ ,  $CC'$  and  $DD'$  orthogonal to fault strikes with differential-curvature data from EGM2008 ( $n_{\max} = 1080$ ) on the left, and from EGM2008 ( $n_{\max} = 2160$ ) on the right. The colour scale is the same as in Fig. 2.

**Table 1.** Parameters of the forward model to be estimated within given fixed bounds (first three rows), and parameters fixed to given values (last two rows).

Location (km)	$0 \leq u_0^{(1)} \leq 100$	$100 \leq u_0^{(2)} \leq 240$	$100 \leq u_0^{(3)} \leq 260$
Dip angle ( $^{\circ}$ )	$90 \leq \chi_1 \leq 170$	$0 \leq \chi_2 \leq 90$	$0 \leq \chi_3 \leq 90$
Upper depth of layer (km)	$-8.3 \leq w_1 \leq -0.5$	$-13 \leq w_2 \leq -0.5$	$-13 \leq w_3 \leq -0.5$
Lower depth of layer (km)	$-8.3$	$-13$	$-13$
Density contrast ( $\text{kg m}^{-3}$ )	$\Delta\rho_1 = 200$	$\Delta\rho_2 = 400$	$\Delta\rho_3 = 200$
			$\Delta\rho_4 = 200$

linearization and is better able to determine the global minimum of a cost function that has many local minima (Uzun and Jekeli 2015). The cost function is defined as the sum of the squared differences between the differential-curvature gradient,  $\Gamma_C$ , computed from EGM2008 and the corresponding gradient predicted by the model described in Fig. 4,

$$\phi(\xi) = \sum_i \left( \Gamma_C^{(\text{EGM2008})}(u_i; \xi) - \Gamma_C^{(\text{model})}(u_i; \xi) \right)^2, \quad (2)$$

where  $u_i$  is the location of the  $i$ th differential curvature along a profile transecting the fault at right angles. The parameter vector,  $\xi$ , consists of the locations of the faults,  $u_0^{(j)}$ , relative to the southwestern endpoint of the profile, the fault dip angles,  $\chi_j$ ,  $j = 1, 2, 3$ , and

possibly the upper boundaries,  $w_k$ ,  $k = 1, \dots, 4$  (Fig. 4). The lower boundaries of the density layers are not estimated but fixed to the values listed in Table 1, roughly consistent with the model determined by Keller and Baldridge (1995). The estimation results are not particularly sensitive to these lower bounds, as verified below.

Inversion of a gravity field model to estimate its parameters by the method of simulated annealing has been accomplished for a variety of applications; for example, by Nagihara and Hall (2001), Roy *et al.* (2005) and Yang *et al.* (2018). Fig. 7 summarizes the simulated annealing algorithm (for details, see Uzun 2013) by showing the essential flow of the logic described below and the computations to obtain the optimal estimates of the parameters. Identifying the cost function as the energy of a system of states defined by the

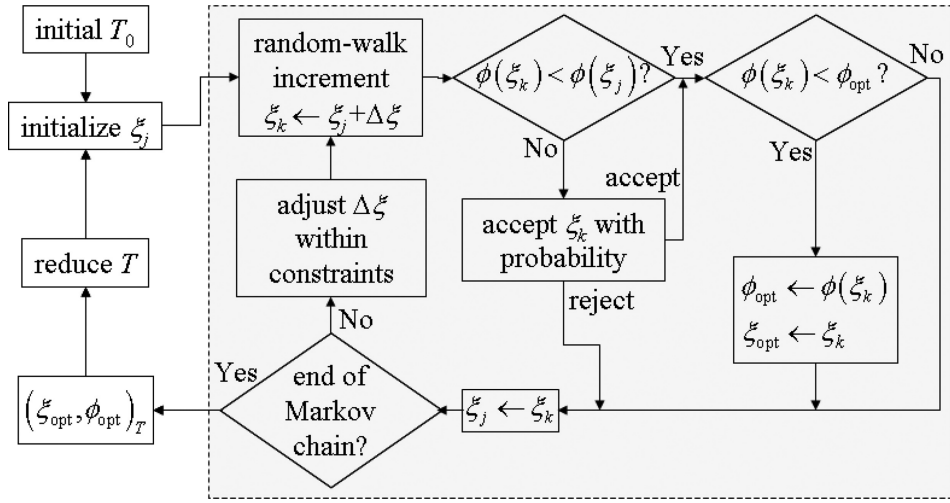


**Figure 7.** Simulated annealing estimation procedure. The shaded part is the Metropolis algorithm that generates a Markov cCain for the candidate parameter that is consistent with the equilibrium energy of the system, but also extracts the parameter for the lowest energy at that temperature. The procedure is terminated if the changes in energy (the cost function) with decreasing temperature are numerically insignificant.

**Table 2.** Nominal parameter values for the model shown in Fig. 4 and used in the sensitivity studies.

Location (km)	$u_0^{(1)} = 130$	$u_0^{(2)} = 200$	$u_0^{(3)} = 220$
Dip angle (°)	$\chi_1 = 154$	$\chi_2 = 30$	$\chi_3 = 30$
Upper depth of layer (m)	$w_1 = -3500$	$w_2 = -3500$	$w_3 = -3500$
Density contrast ( $\text{kg m}^{-3}$ )	$\Delta\rho_1 = 200$	$\Delta\rho_2 = 400$	$\Delta\rho_3 = 200$ $\Delta\rho_4 = 200$

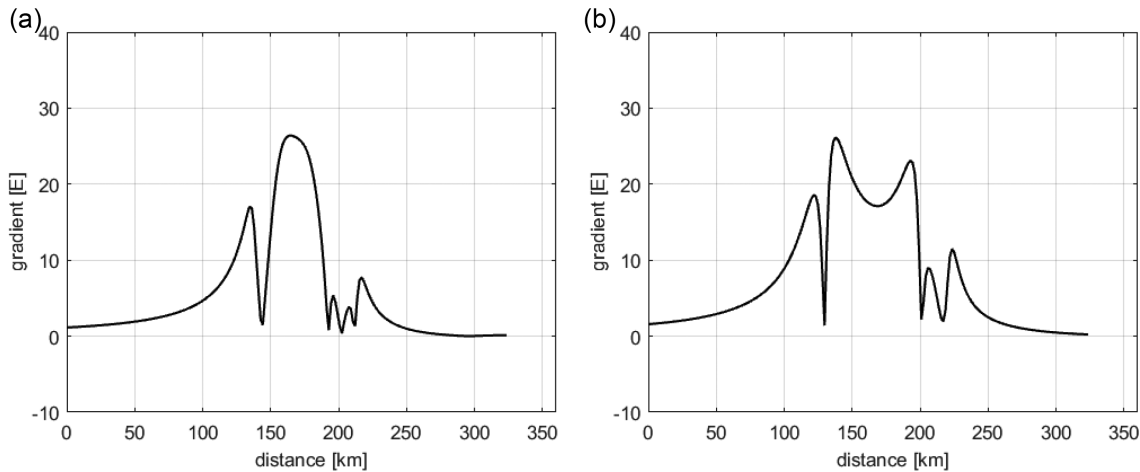


**Figure 8.** The differential-curvature gradient,  $\Gamma_C$ , for the fault model (Fig. 4) using (a) the parameter values of Table 2, and (b) changing all dip angles to  $90^\circ$ .

parameters, the objective is to seek those parameter values that minimize the energy. This is accomplished in stages of systematically decreasing ‘temperatures’ of the system and finding, at each stage, the best parameters of the system that correspond to this intermediate equilibrium. From statistical mechanics, it is known that for a system in thermal equilibrium the Gibbs–Boltzmann distribution describes the probabilities of the states of the system. Thus,

$$\text{Prob}(\xi = \hat{\xi}) \sim e^{-\frac{\phi(\xi)}{T}}, \quad (3)$$

where Boltzmann’s constant is incorporated in the temperature parameter,  $T$ . A representative state of the system is obtained iteratively from some initial state according to a Markov cCain that generates a sample from a stationary process having the Gibbs–Boltzmann distribution. This is the Metropolis algorithm (shaded area

in Fig. 7) whereby subsequent parameter candidates in the chain are perturbed in a way that is consistent with their probabilistic fluctuations as modelled by the system in a state of thermal equilibrium. At each step in the chain, a new candidate is accepted if, compared to the previous candidate, it produces a lower energy of the system, but it is accepted only with probability if it does not. Mathematically, for a random walk chain, if  $P_j$  is the probability that the state is represented by the candidate,  $\xi_j$ , while  $P_k$  is the corresponding probability of the subsequent state of the system, then the probability of accepting the new candidate is given by the Metropolis acceptance ratio (Chib and Greenberg 1995),

$$\alpha = \min \left( 1, \frac{P_k}{P_j} \right) = \min \left( 1, e^{-\frac{\phi(\xi_k) - \phi(\xi_j)}{T}} \right). \quad (4)$$

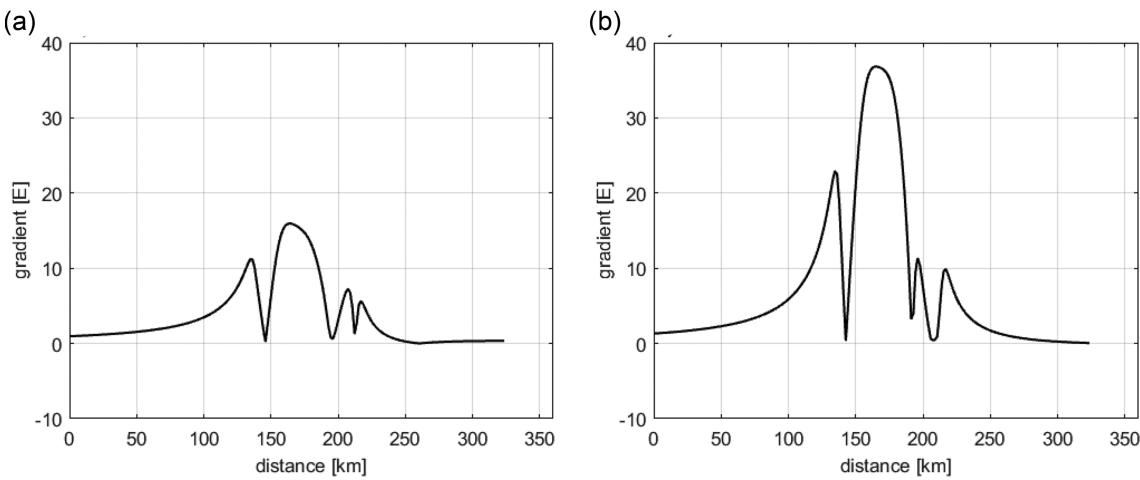


**Figure 9.** The differential-curvature gradient,  $\Gamma_C$ , with either  $300 \text{ kg m}^{-3}$  density contrast between (a) the Burch and Meers faults or (b)  $500 \text{ kg m}^{-3}$  density contrast.

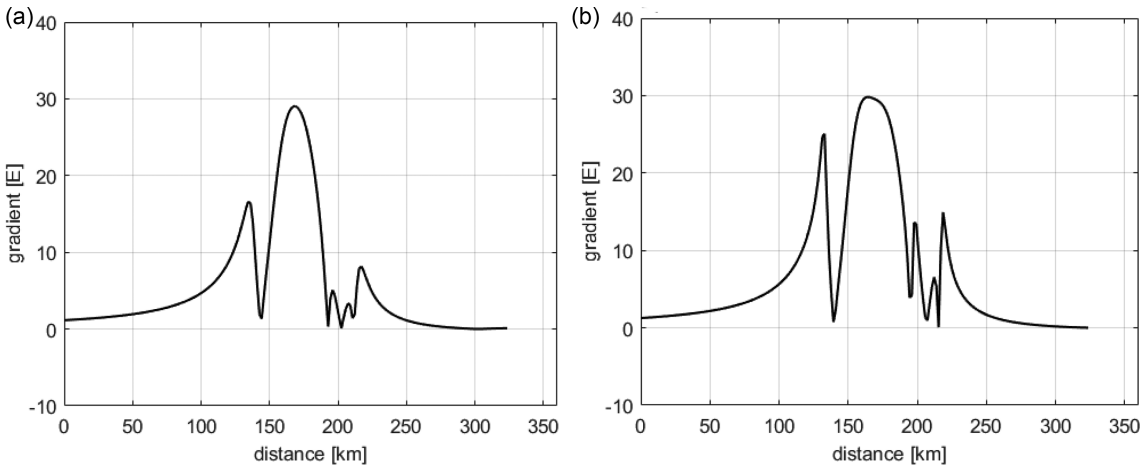


**Figure 10.** The differential-curvature gradient,  $\Gamma_C$ , for the fault model (Fig. 4) and nominal parameter values (Table 2) changed in turn to (a) to greater depths of the lower boundaries of the contrasts; and (b) to shallower depths for the upper boundaries of the contrasts.

**Table 3.** Estimated parameters of the single-fault model using differential-curvature values from EGM2008 ( $n_{\max} = 1080$ ) on Profile  $AA'$  crossing the Burch fault. Bold values are not estimated, but fixed to the nominal values in Table 2. Also, the density contrasts are fixed to the values listed in Table 2.  $\xi_H$  and  $\xi_L$  are upper and lower boundary values for the parameters. Temperature reduction rate is  $\rho = 0.80$

Test 3.n	Initial temperature ( $T$ )	Initial values $\xi$	Parameters $u_0^{(1)}(\text{km}), \chi_1(\text{°}), w_1(\text{m}), w_2(\text{m})$	Cost ( $E^2$ )
1	1000E <sup>2</sup>	$\xi_L + 1.0(\xi_H - \xi_L)$	54.77, 155.2, <b>-3500, -3500</b>	475.29
2	1000E <sup>2</sup>	$\xi_L + 0.8(\xi_H - \xi_L)$	54.77, 155.2, <b>-3500, -3500</b>	475.29
3	1000E <sup>2</sup>	$\xi_L + 0.1(\xi_H - \xi_L)$	54.77, 155.2, <b>-3500, -3500</b>	475.29
4	1000E <sup>2</sup>	$\xi_L + 0.01(\xi_H - \xi_L)$	54.77, 155.2, <b>-3500, -3500</b>	475.29
5	10000E <sup>2</sup>	$\xi_L + 1.0(\xi_H - \xi_L)$	54.97, 155.4, -3271, -3271	472.09
6	10000E <sup>2</sup>	$\xi_L + 0.1(\xi_H - \xi_L)$	54.97, 155.4, -3271, -3271	472.09
7	10000E <sup>2</sup>	$\xi_L + 0.8(\xi_H - \xi_L)$	54.97, 155.4, -3271, -3271	472.09
8	10000E <sup>2</sup>	$\xi_L + 0.01(\xi_H - \xi_L)$	54.97, 155.4, -3271, -3271	472.09

If the energy with the new candidate is less than the energy with the previous candidate ( $\phi(\xi_k) - \phi(\xi_j) < 0$ ), then the new candidate is accepted with probability one (i.e. definitely). Otherwise, it is accepted only with the given probability, which becomes less likely as the temperature of the system decreases. Convergence to the global minimum is guaranteed under general conditions if the rate of temperature reduction is sufficiently gradual (Geman and Geman 1984). The length of the Markov Chain in our case is a fixed parameter of the algorithm. A particular fault model parameter can be

fixed (i.e. not estimated) by constraining its increments to be null within the Metropolis algorithm. The intermediate candidates for the parameter values are not allowed to wander outside reasonable established bounds listed in Table 1.

The search domains for the parameters are set to the values taking into account the geometry of the fault and geological information. For example, the search domain for the upper depth levels of the density contrasts cannot be set less than the lower levels given in Table 1. The search domains for the location parameters are set

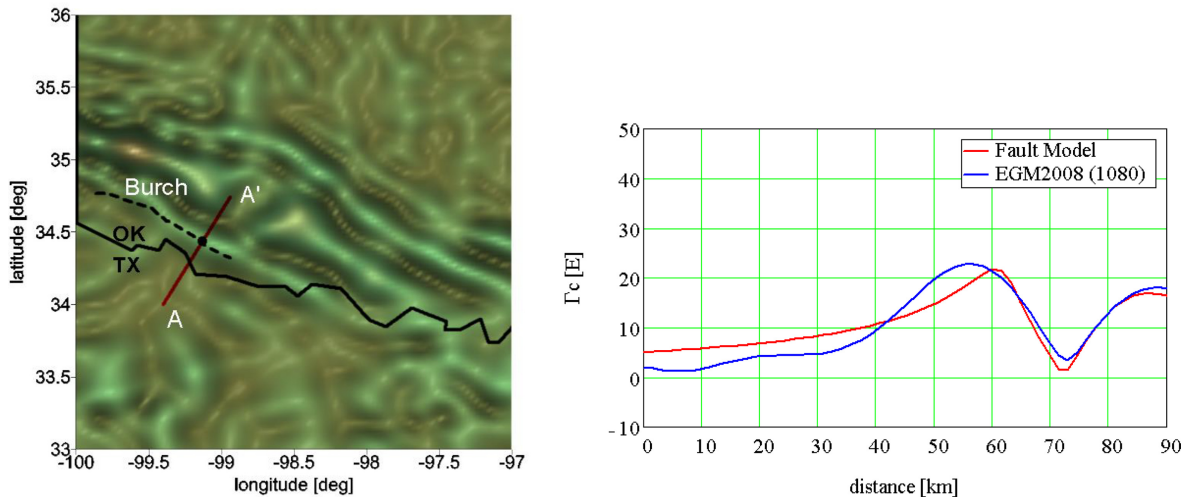


**Figure 11.** Estimated location (black dot in left-hand panel) of the Burch Fault based on EGM2008 ( $n_{\max} = 1080$ ) differential-curvature data along Profile  $AA'$  using a single-fault model. The colour scale is the same as in Fig. 2. The right-hand panel compares the fitted model to the data.

**Table 4.** Estimated parameters of the multiple-fault models using differential-curvature values from EGM2008 ( $n_{\max} = 2160$ ) along Profiles  $CC'$  and  $DD'$ . The density contrasts are fixed to the values of Table 2, and the corresponding depths are fixed to values that give optimal fits to the model.

	$CC'$ (two-fault model)	$CC'$ (three-fault model)	$DD'$
$u_0^{(1)}$ (km)	60.49	60.56	–
$u_0^{(2)}$ (km)	–	158.0	51.88
$u_0^{(3)}$ (km)	159.4	131.4	34.14
$\chi_1$ (°)	135.3	135.0	–
$\chi_2$ (°)	–	22.0	42.63
$\chi_3$ (°)	16.3	39.4	26.56
$w_1$ (m)	–3500	–3500	–
$w_2$ (m)	–	–3500	–2500
$w_3$ (m)	–3500	–3500	–2500
$w_4$ (m)	–6000	–6000	–5000
Cost ( $E^2$ )	3534.7	2748.8	3892.9

to the values relative to the endpoint of the profiles to cover the reasonable location values along the profile. One could increase the search space, but at the cost of increased computation time.

#### 4 NUMERICAL RESULTS

Preliminary numerical investigations show that the gravitational gradients of model, Fig. 4, are most sensitive, among the parameters to be solved, to variations in the dip angles. Table 2 lists the nominal parameter values for  $u_0^{(j)}$ ,  $\Delta\rho_k$  and  $w_k$ , that are used in these preliminary calculations of the forward modelled differential-curvature gradient,  $\Gamma_C$ .

Fig. 8 shows that the gradient profiles differ significantly for the dip-angle combinations, ( $\chi_1 = 154^\circ$ ,  $\chi_2 = \chi_3 = 30^\circ$ ) and ( $\chi_1 = \chi_2 = \chi_3 = 90^\circ$ ), and where the lower boundaries of the density layers are the values indicated in Table 1. Indeed, a comparison of Fig. 8 to the general variation across the faults indicated by the EGM2008 model suggests low-angle faults rather than high-angle faults. For the possible extremes in density contrast of the central ‘mafic intrusion’ between the Burch and Meers faults,  $300 \text{ kg m}^{-3} \leq \Delta\rho_2 \leq 500 \text{ kg m}^{-3}$ , the consequent gradients,

$\Gamma_C$ , using the nominal values for all other parameters, differ primarily in scale (Fig. 9). Finally, we consider variations in the depths of the upper and lower boundaries of the layers. They are changed in unison, either lowering the lower boundaries by 2 km or raising the upper boundaries by 2 km. Figs 10(a) and (b) show both cases, indicating again that these primarily change the magnitude of the overall signal (though not with uniform scale). In fact, changes in the lower boundaries have practically no effect (compare Figs 8a and 10a).

The EGM2008 differential-curvature gradients (Appendix A) are computed along the three Profiles,  $AA'$ ,  $CC'$  and  $DD'$ , shown in Fig. 6 crossing the Burch, Waurika–Muenster, Meers, Mountain View and Duncan–Criner Faults. These gravitational ‘data’ on Profile  $AA'$  appear most distinct in relation to the Burch Fault when low-pass filtered by truncating the EGM2008 model at degree  $n = 1080$ . The full spherical harmonic model up to degree  $n = 2160$  is used as data on Profiles  $CC'$  and  $DD'$ .

Estimates for the fault model parameters described in Fig. 4 and obtained by the method of simulated annealing are listed in Tables 3 and 4, as described below. Analysis of the robustness of the method is also presented. The location parameter value is relative to the southwestern end of the profile and indicate where the fault plane of the model intersects ground level. How the gradient signatures due to the density contrasts on either side of the fault combine in relation to the location of the fault is illustrated for the Burch Fault in Fig. B.2 (Appendix B).

In Table 3, the tests 3.1–3.8 demonstrate the results of the SA algorithm and corresponding final cost functions under different initial temperatures,  $T$ , and different starting values for the parameters. The estimated parameters fit very well the nominal values inferred from the structural model of Keller and Baldridge (1995). Nearly the same values are obtained if the depths of the density contrasts are estimated in addition to the dip angle and location parameter. All three estimates are robust since they are essentially invariant with respect to initial parameter values and thus also yield convergence of the cost function to the same final value. Also, the estimated location of the fault agrees with the mapped location as shown in Fig. 11; and indeed, the model overall fits well to the data. For any particular estimation problem, some experimentation is usually required to ensure a robust estimation since an initial temperature that is too low may cause the algorithm to miss the

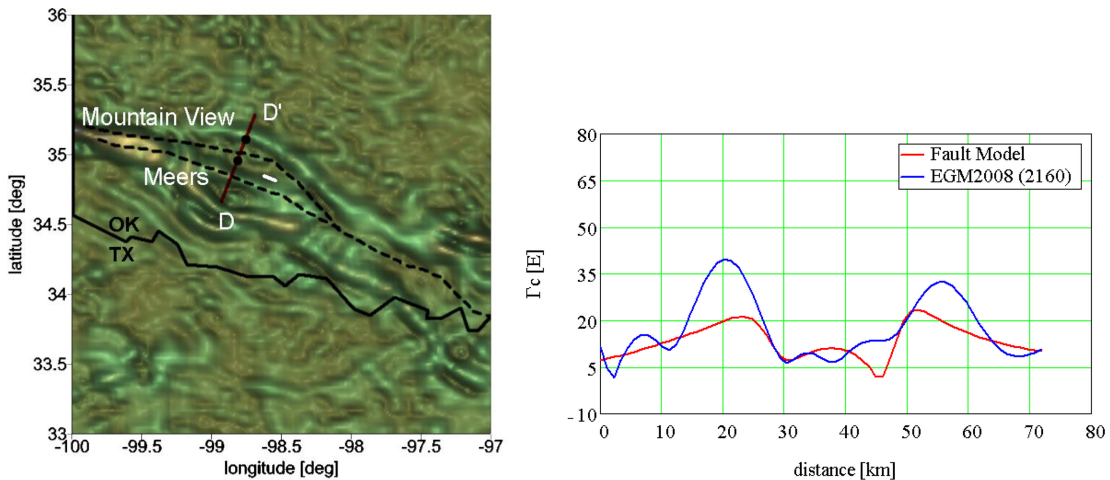


**Figure 12.** Estimated locations (left-hand panel) of the Meers and Mountain View Faults based on EGM2008 ( $n_{\max} = 2160$ ) differential-curvature data along Profile  $DD'$  using a two-fault model. The black dots identify the estimated locations and the white line segment corresponds to the Meers Fault that is physically visible on Google Earth imagery. The colour scale is the same as in Fig. 2. The right-hand panel compares the fitted model to the data.

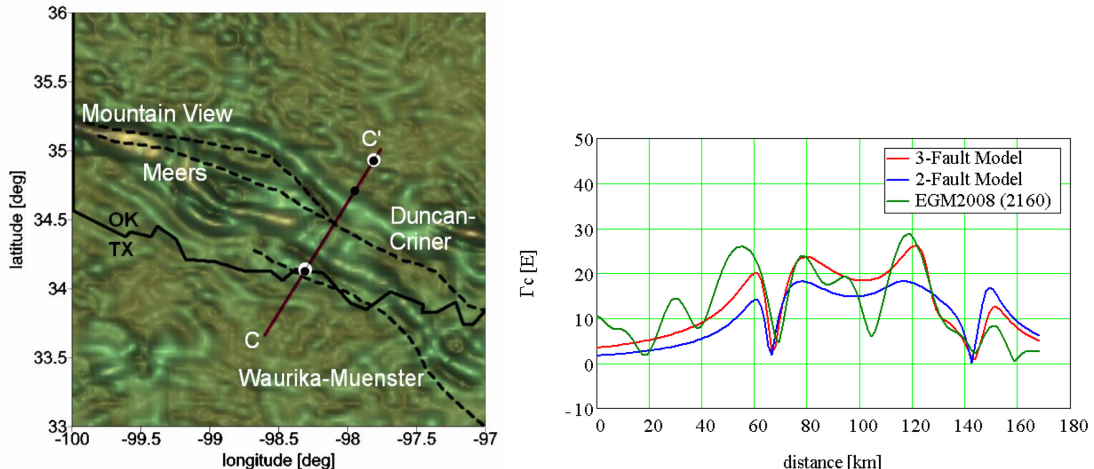


**Figure 13.** Left: estimated locations of faults using EGM2008 ( $n_{\max} = 2160$ ) data on Profile  $CC'$  and either a two-fault model (larger white dots) or a three-fault model (smaller black dots). The colour scale is the same as in Fig. 2. Right: differential-curvature gradients along Profile  $CC'$  according to EGM2008 ( $n_{\max} = 2160$ ) and compared to the fitted two- and three-fault models.

global minimum of the cost function. For example, starting with some initial temperature, such as  $T = 1$ , its value is varied until the different initial parameter values converge to the same final cost function. Besides this, an appropriate temperature reduction rate between  $[0,1]$  must also be chosen. Typical values of the rate for reasonably slow cooling range between 0.5 and 0.95. A FORTRAN source code implementation of the SA algorithm to estimate parameters of the Burch fault is provided on GitHub and available at [https://github.com/geodesy00/SAfault\\_inversion.git](https://github.com/geodesy00/SAfault_inversion.git)

Table 4 summarizes the estimation results for the location and the dip angle of the multiple fault model using the Profiles,  $CC'$  crossing the Waurika–Muenster and Duncan–Criner Faults, and  $DD'$  crossing the Meers and Mountain View Faults, for the highest resolution of the EGM2008 gradients. Fig. 12 shows the estimated locations of the Meers and Mountain View Faults on the  $DD'$  profile relative to the mapped faults of Fig. 1(a). The search spaces for the location parameters in this case are set to  $0 \text{ km} \leq u_0^{(2)} \leq 240 \text{ km}$  and  $0 \text{ km} \leq u_0^{(3)} \leq 260 \text{ km}$ . Similar robustness analyses as in Table 3 have been performed also in these cases, although the model does

not fit as well due to the increased resolution of the data. Particularly interesting, however, is the significant discrepancy between estimated and mapped fault location, especially since the estimated Meers location appears to agree quite well with the physically observed location (Google Earth imagery; see also the aerial views shown by Madole 1988). It is further interesting that the best fit of the model to the EGM2008 data actually reverses the order of the faults, where the location of fault 2, indicated by the parameter,  $u_0^{(2)}$ , is further from the start point of the profile than the location of fault 3 (i.e.  $u_0^{(3)} < u_0^{(2)}$ ). It is believed that the SA optimization procedure in this case is compensating for specified (i.e. assumed) density contrasts that are significantly different from actual values.

Finally, Fig. 13 shows the estimation results for the EGM2008 ( $n_{\max} = 2160$ ) differential-curvature data on Profile  $CC'$ . Both two- and three-fault models are considered. In this case, the search spaces for the dip angle and the location parameters are set to  $10^\circ \leq \chi_2 \leq 90^\circ$ ,  $10^\circ \leq \chi_3 \leq 90^\circ$ ,  $100 \text{ km} \leq u_0^{(2)} \leq 170 \text{ km}$ , and  $100 \text{ km} \leq u_0^{(3)} \leq 170 \text{ km}$ , and the search spaces of the other parameters are set as in Table 1. Again, there is agreement between the

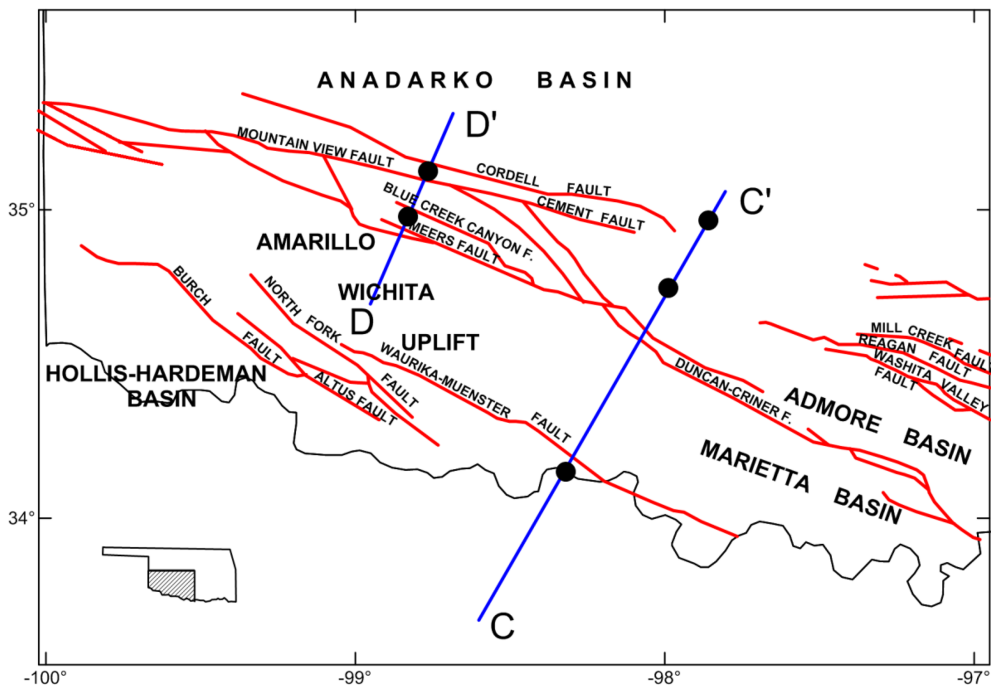


**Figure 14.** A map of the faults in the Wichita Uplift region according to Luza *et al.* (1987). The black dots show the EGM2008-estimated locations of the modelled faults on Profiles  $DD'$  and  $CC'$ .

estimated and mapped locations of the Waurika–Muenster Fault; but, there is a strong discrepancy in the location of the Duncan–Criner Fault, analogous to the apparent discrepancies on Profile  $DD'$  (Fig. 12). As for Profile  $DD'$ , the fitted models do not agree as well with the data, and the three-fault model is only marginally better than the two-fault model. It is noted that as the number of faults in the model increases (as the number of parameters in the estimation problem increases) the robustness decreases. On the other hand, it is possible with many trials to achieve much better fits by allowing the depths as well as the density contrasts to be estimated (although, as is often the case, over-parametrization leads to better fits but likely less reasonable physics). Again, as for Profile  $DD'$ , one consistently obtains a reversal in the order of locations of faults 2 and 3 ( $u_0^{(3)} < u_0^{(2)}$ ) in the three-model estimation.

The discrepancies between mapped faults and their EGM2008-estimated locations may be explained in one or more ways. In the first place, the geology, especially toward the northeast of the uplift, is significantly more complex than to the southwest, thus possibly significantly invalidating the model used in the estimation. Another reason may be that some of the faults are mapped from surface observations while the gravity model reflects the deeper geological structure; and, as indicated in Chang *et al.* (1989), the faults may be curved rather than planar (although this would not explain the Meers Fault discrepancy). A third explanation is that the gravity model selects gravitationally more significant faults, while the mapped faults are selected on another distinguishing basis—both the map from (Keller and Baldridge 1995; abridged in Fig. 1) and the one shown in Fig. 14 from Luza *et al.* (1987) show many parallel faults north of the uplift and the particular faults identified by the gravity model are not necessarily obvious. Finally, a comparison of the Keller–Baldridge and Luza-*et-al.* maps also shows some location discrepancies, which leads to the final reason that these maps are meant to be rather more schematic than coordinate accurate, giving a general layout of the faults in the region instead of a delineation faithful to a standard coordinate system.

A general remark on the uncertainties in the estimated parameters, dip angle and fault location, should also be made. Formal uncertainty values could definitely be given on the basis of the least-squares estimation, assuming that the observation uncertainties are known. However, they would have little meaning because, as in most studies of this kind, the accuracy of the estimates is dominated completely by (non-random) model error. First, it is assumed that the faults can be represented as infinitely extended planes with a single dip angle and with a strike direction that is surmised visually from the plotted lineaments indicated by the differential curvature of the field. The second main assumption is that the forward model for the gravitational gradients is based on one or more horizontal density contrasts at constant depths, where the values of the contrasts and depths are inferred from models derived by others on the basis of local gravity, seismic and bore-hole data. These model simplifications, amounting to model error, imply that we can only provide a qualitative result, not parameter estimates with meaningful accuracy bounds.

## 5 CONCLUSION

Several studies of the Wichita Uplift in association with the SOA over the last six decades have modelled the major faults that bound this region to the north and south using surface geology, well data, seismic reflection surveys, magnetic and gravimetric data. Although the seismic studies rather conclusively show a low-angle structural geology, the early models also indicated high-angle faults. Using the recent comprehensive and detailed gravity model, EGM2008, and corresponding derived gravitational gradients that represent the differential curvature of the field, we find consistency with the low-angle fault model. This is demonstrated through an optimal estimation process known as simulated annealing that is able to find the global least-squares minimum of the cost function for a model that is nonlinear in the parameters, including dip angle, fault

location and possibly their depths. Only the gravitational gradients are used to estimate these parameters. Based on inferred values (Brewer *et al.* 1983; Keller and Stephenson 2007), the estimated dip angles appear reasonable for all faults. Agreement is also found between the estimated and previously mapped locations of the Burch and Waurika–Muenster Faults. However, significant discrepancies are indicated between the estimated and mapped locations of the Meers, Mountain View and Duncan–Criner Faults, although there is agreement with the physically visible Meers Fault. These discrepancies could be explained on the basis of geological complexity not included in the models. However, the models derived here together with the demonstrated estimation procedure may lead to further model refinement and expansion, including the introduction of non-gravitational constraints to improve the solution to this inverse problem. Of particular note in this respect is the high-resolution rendition of linear features such as geological faults that is enabled using the differential field curvature.

Moreover, the presented method can be applied for many problems of geophysics where knowledge of the fault attitude is of prime importance. In tectonic settings where reverse and normal faults are present, the estimation method can be used to constrain the dip angle as well as the location. Potential applications include fault-related geothermal systems for finding hot fluids and fault-trap type reservoirs in oil/gas studies. In earthquake studies, the knowledge of the fault plane geometry is needed for modelling tectonic stress change during earthquakes. The illustrated method of estimation may lead to improved models of active faults.

## ACKNOWLEDGEMENTS

The authors are grateful for several comments by Randy Keller, an anonymous reviewer, and the editor that improved the manuscript.

## REFERENCES

- Brewer, J.A., 1982. Study of Southern Oklahoma Aulacogen, using CO-CORP deep seismic-reflection profiles, *Oklahoma Geol. Surv. Guidebook*, **21**, 31–39.
- Brewer, J.A., Good, R., Oliver, J.E., Brown, L.D. & Kaufman, S., 1983. CO-CORP profiling across the Southern Oklahoma aulacogen: overthrusting of the Wichita Mountains and compression within the Anadarko Basin, *Geology*, **11**, 109–114.
- Chang, W.F., McMechan, G.A. & Keller, G.R., 1989. Wave field processing of data from a large-aperture seismic experiment in Southwestern Oklahoma, *J. geophys. Res.*, **94**(B2), 1803–1816.
- Chib, S. & Greenberg, E., 1995. Understanding the Metropolis-Hastings algorithm, *Am. Stat.*, **49**(4), 327–335.
- Coffman, J.D., Gilbert, M.C. & McConnell, D.A., 1986. An interpretation of the crustal structure of the southern Oklahoma aulacogen satisfying gravity data, *Oklahoma Geol. Surv. Guidebook*, **23**, 1–10.
- Farr, T.G. *et al.*, 2007. The Shuttle Radar Topography Mission, *Rev. Geophys.*, **45**, RG2004.
- Gay, S.P., 2014. Some observations on the Amarillo/Wichita Mountains thrust-fold belt and its extensions Southeast into east Texas and northwest into New Mexico, *J. Oklahoma City Geol. Soc.*, **65**(5), 338–366.
- Geman, S. & Geman, D., 1984. Stochastic relaxation, Gibbs distribution and the Bayesian restoration in images, *IEEE Trans. Patt. Anal. Mac. Intel.*, **6**(6), 721–741.
- Gilbert, M.C., 1983. Timing and chemistry of igneous events associated with the Southern Oklahoma Aulacogen, *Tectonophysics*, **94**, 439–455.
- Ham, W.E., Denison, R.E. & Merritt, C.A., 1964. Basement rocks and structural evolution of southern Oklahoma, *Oklahoma Geol. Surv. Bull.*, **95**, 1–302.
- Hamilton, L.S., 1989. Structure of the Wichita uplift, Southern Oklahoma, from a wide-angle seismic experiment, MS thesis, Univ. of Texas El Paso, 69 pp.
- Heiland, C.A., 1940. *Geophysical Exploration*. Prentice-Hall, New York.
- Hoffman, P., Dewey, J.F. & Burke, K., 1974. Aulacogens and their genetic relation to geosynclines, with a Proterozoic example from great Slave lake, Canada, In: Dott, R.H. & Shaver, R.H.(eds.), *Modern and Ancient Geosynclinal Sedimentation*. Society of Economic Paleontologists and Mineralogists Special Publication, **Vol. 19**, pp. 38–55.
- Hofmann-Wellenhof, B. & Moritz, H., 2005. *Physical Geodesy*. Springer Verlag, Berlin.
- Jekeli, C., 2015. Potential theory and static gravity field of the Earth, *Treatise on Geophysics*, 2nd edition, Schubert, G(ed.), Vol. 3, pp. 9–35. Elsevier Publ., Oxford.
- Jordan, S.K., 1978. Statistical model for gravity, topography, and density contrasts in the Earth, *J. geophys. Res.*, **83**(B4), 186–1824.
- Keller, G.R. & Baldrige, W.S., 1995. *The Southern Oklahoma Aulacogen*. In: Olsen, K.H.(ed.), Continental Rifts: Evolution, Structure, Tectonics, pp. 427–435.
- Keller, G.R. & Stephenson, R.A., 2007. The Southern Oklahoma and Dnieper-Donets aulacogens: a comparative analysis, *Geol. Soc. Am. Mem.*, **200**, 127–143.
- Luza, K.V., Madole, R.F. & Crone, A.J., 1987. Investigation of the Meers fault, Southwestern Oklahoma, Oklahoma Geological Survey Special Publication 87-1, pp. 1–75.
- Madole, R., 1988. Stratigraphic evidence of Holocene faulting in the mid-continent: the Meers fault, southwestern Oklahoma, *Bull. geol. Soc. Am.*, **100**, 392–401.
- Murphy, C.A. & Brewster, J., 2007. Target delineation using full tensor gravity gradiometry data, ASEG 2007, Perth, Australia, Extended Abstracts, pp. 1–3.
- Nagihara, S. & Hall, S.A., 2001. Three dimensional gravity inversion using simulated annealing: constraints on the diapiric roots of allochthonous salt structures, *Geophysics*, **66**(5), 1340–1649.
- Papesh, H., 1983. A regional geophysical study of the Southern Oklahoma Aulacogen, MS thesis, University of Texas, El Paso.
- Pavlis, N.K., Holmes, S.A., Kenyon, S.C. & Factor, J.F., 2012. The development and evaluation of Earth Gravitational Model (EGM2008), *J. geophys. Res.*, **117**, B04406, doi:10.1029/2011JB008916.
- Perry, W.J., 1989. Tectonic evolution of the Anadarko basin, *U.S. Geological Survey Bulletin*, no. 1866-A, US Geological Survey.
- Pruatt, M.A., 1974. The Southern Oklahoma Aulacogen: a geophysical and geological investigation, M.S. Thesis, Univ. of Oklahoma, Norman, OK.
- Reed, G.B., 1973. Application of kinematical geodesy for determining the short wave length components of the gravity field by satellite gradiometry, Report no. 201, Department of Geodetic Science, Ohio State University, Columbus, OH.
- Robbins, S.L. & Keller, G.R., 1992. Complete Bouger and isostatic residual maps of the Anadarko basin, Wichita Mountains, and surrounding areas, Oklahoma, Kansas, Texas, and Colorado, *U.S. Geol. Surv. Bull.*, 1866 G, pp. G1–G11.
- Roy, L., Sen, M.K., Blankenship, D.D., Stoffa, P.L. & Richter, T.G., 2005. Inversion and uncertainty estimation of gravity data using simulated annealing: an application over Lake Vostok, East Antarctica, *Geophysics*, **70**(1), J1–J12.
- Teunissen, P., 1990. Nonlinear least-squares, *Manuscr. Geod.*, **15**, 137–150.
- Uzun, S., 2013. Estimating parameters of subsurface structures from airborne gravity gradiometry data using a Monte-Carlo Optimization Method, Report no. 506, Geodetic Science, Ohio State University, OH, available at: <http://earthsciences.osu.edu/sites/earthsciences.osu.edu/files/report-506.pdf>, last accessed in 9 June 2020.
- Uzun, S. & Jekeli, C., 2015. Comparison of least-squares and simulated annealing to estimate fault parameters from airborne gravity gradiometry, *Stud. Geophys. Geod.*, **59**, 21–50.
- Wickham, J., 1978. The Southern Oklahoma Aulacogen, In: *Structures and Stratigraphy of the Ouachita Mountains and the Arkoma Basin, Field Guide*, pp. 1–59; Oklahoma City Geological Society.

- Yang, J., Jekeli, C. & Liu, L., 2018. Seafloor topography estimation from gravity gradients using simulated annealing, *J. geophys. Res.*, **123**, 6958–6975.

## APPENDIX A: EGM2008 BOUGUER ANOMALIES AND DIFFERENTIAL FIELD CURVATURE

The EGM2008 (Pavlis *et al.* 2012) represents the global gravitational potential as a finite series of spherical harmonic functions,  $\bar{Y}_{n,m}$ . Removing an ellipsoidal reference field, the residual, also known as the disturbing potential, is given by (Hofmann-Wellenhof and Moritz 2005; Jekeli 2015),

$$T(r, \theta, \lambda) = \frac{GM}{a} \sum_{n=2}^{n_{\max}} \left(\frac{a}{r}\right)^{n+1} \sum_{m=-n}^n \delta C_{n,m} \bar{Y}_{n,m}(\theta, \lambda), \quad (\text{A1})$$

where  $(r, \theta, \lambda)$  are spherical polar coordinates (radius, colatitude and longitude),  $GM$  is Newton's gravitational constant times Earth's mass,  $a$  is the spherical radius (set equal to the semi-major axis of an Earth-fitting ellipsoid) to which the residual harmonic coefficients,  $\delta C_{n,m}$ , refer. The free-air gravity anomaly is related to  $T$  according to  $\Delta g = -\partial T / \partial r - 2T/r$ , and is readily computed from the corresponding series,

$$\begin{aligned} \Delta g(r, \theta, \lambda) = & \frac{GM}{a^2} \sum_{n=2}^{n_{\max}} (n-1) \left(\frac{a}{r}\right)^{n+2} \\ & \times \sum_{m=-n}^n \delta C_{n,m} \bar{Y}_{n,m}(\theta, \lambda). \end{aligned} \quad (\text{A2})$$

The local Bouguer anomaly is defined by  $\Delta g_B = \Delta g - 2\pi\rho Gh$ , using a nominal crust density,  $\rho = 2670 \text{ kg m}^{-3}$ , and where  $h$  is topographic height. The spherical harmonic expansion of  $h$ , DTM2006 (Pavlis *et al.* 2012), that accompanies EGM2008, is used with eq. (A2) to compute the Bouguer anomalies in Fig. 1(c).

The residual gravitational gradients,  $\Gamma_{j,k}$ , form a second-order symmetric tensor of second partial derivatives of the disturbing potential,  $\partial^2 T / (\partial x_j \partial x_k)$ , with respect to local Cartesian coordinates,  $(x_1, x_2, x_3)$ , where the indices denote directions,  $(1, 2, 3) \equiv$  (north, east, down). The relationships to the derivatives with respect to the spherical coordinates are (Reed 1973)

$$\Gamma_{1,1} = \frac{1}{r} \frac{\partial T}{\partial r} + \frac{1}{r^2} \frac{\partial^2 T}{\partial \theta^2} \quad (\text{A3})$$

$$\Gamma_{1,2} = \frac{\cot \theta}{r^2 \sin \theta} \frac{\partial T}{\partial \lambda} - \frac{1}{r^2 \sin \theta} \frac{\partial^2 T}{\partial \theta \partial \lambda} \quad (\text{A4})$$

$$\Gamma_{1,3} = -\frac{1}{r^2} \frac{\partial T}{\partial \theta} + \frac{1}{r} \frac{\partial^2 T}{\partial \theta \partial r} \quad (\text{A5})$$

$$\Gamma_{2,2} = \frac{\cot \theta}{r^2} \frac{\partial}{\partial \theta} + \frac{1}{r} \frac{\partial}{\partial r} + \frac{1}{r^2 \sin^2 \theta} \frac{\partial^2}{\partial \lambda^2} \quad (\text{A6})$$

$$\Gamma_{2,3} = \frac{1}{r^2 \sin \theta} \frac{\partial T}{\partial \lambda} - \frac{1}{r \sin \theta} \frac{\partial^2 T}{\partial \lambda \partial r} \quad (\text{A7})$$

$$\Gamma_{3,3} = \frac{\partial^2 T}{\partial r^2} \quad (\text{A8})$$

Thus, the local gravitational gradients are computed directly from the EGM2008 model by applying the appropriate analytical derivatives to eq. (A1).

The curvature of any twice-differentiable surface may be characterized at a point on the surface by two principal radii of curvature,  $\xi_1'$ ,  $\xi_2'$ . The difference in the principal curvatures of a surface of constant potential is related to the gravitational gradients according to (Heiland 1940, p.170 ff.)

$$\left| \frac{1}{\xi_2'} - \frac{1}{\xi_1'} \right| = \frac{1}{g_3} \sqrt{(2\Gamma_{1,2})^2 + (\Gamma_{2,2} - \Gamma_{1,1})^2} = \frac{\Gamma_C}{g_3}, \quad (\text{A9})$$

where  $g_3$  is the vertical gravitational acceleration, which is taken as a constant. This 'differential-curvature' gradient,  $\Gamma_C$ , is invariant with respect to coordinate rotation about the vertical axis and is particularly interesting in geology as it identifies lineaments, or sharp horizontal contrasts in the structure of the source mass density (Murphy and Brewster 2007).

The cross-strike derivative of the vertical gradient of the potential (the cross-strike gradient of gravity) is obtained for a given strike direction by rotating the gravity gradient tensor so that one axis lies orthogonal the strike direction. Let a new local coordinate system be defined by the axes,  $u$ ,  $v$ ,  $w$ , where  $u$  is orthogonal to the strike direction and  $w$  is in the vertical (upward), parallel to  $x_3$ . Let the cross-strike direction be defined by the azimuth,  $\alpha$ , which is the angle from north to the  $u$ -axis. Starting with the local northeast-down coordinate system, a rotation about the vertical axis by the angle,  $\alpha$ , brings the  $x_1$ -axis orthogonal to the strike, and the  $x_2$ -axis parallel to it. The gradient tensor transforms according to

$$\Gamma^{u,v,w} = \mathbf{R}_3(\alpha) \Gamma \mathbf{R}_3^T(\alpha), \quad (\text{A10})$$

where the rotation matrix is

$$\mathbf{R}_3(\alpha) = \begin{pmatrix} \cos \alpha & \sin \alpha & 0 \\ -\sin \alpha & \cos \alpha & 0 \\ 0 & 0 & 1 \end{pmatrix}; \quad (\text{A11})$$

and, consequently, the cross-strike gradient of gravity is  $\Gamma_{u,w}$ , given by

$$\Gamma_{u,w} = \Gamma_{1,3} \cos \alpha + \Gamma_{2,3} \sin \alpha = \Gamma_{3,1} \cos \alpha + \Gamma_{3,2} \sin \alpha. \quad (\text{A12})$$

## APPENDIX B: GRAVITATIONAL GRADIENTS FOR A DIP-SLIP FAULT

The dip-slip fault is modelled as a semi-infinite plane below ground level that is infinite in both directions of the strike (Fig. B.1). A layered density contrast is assumed on either side at different depths, as shown in the Fig. B.1, where the  $w$ -axis is the third axis in a local coordinate system with one horizontal axis along the strike of the fault. The following formulas give the  $\Gamma_{w,w}$  gravitational gradient, using the notation defined in Fig. B.1 (Uzun 2013). The contributions to  $\Gamma_{ww}$  due to the density contrasts,  $\Delta\rho^{(L)}$  and  $\Delta\rho^{(R)}$ , respectively located to the left- and right-hand sides of the fault, are

$$\Gamma_{ww}^{(L)}(u, w) = 2G\Delta\rho^{(L)} (A^{(L)} \cos \chi - D^{(L)}E) \sin \chi, \quad (\text{B1})$$

$$\Gamma_{ww}^{(R)}(u, w) = -2G\Delta\rho^{(R)} (A^{(R)} \cos \chi - D^{(R)}E) \sin \chi, \quad (\text{B2})$$

where

$$A^{(L,R)} = \frac{F_2^{(L,R)} \theta_2^{(L,R)} - F_1^{(L,R)} \theta_1^{(L,R)}}{E \sin \chi} - \frac{1}{2} \ln \frac{G_1^{(L,R)}}{G_2^{(L,R)}}, \quad (\text{B3})$$

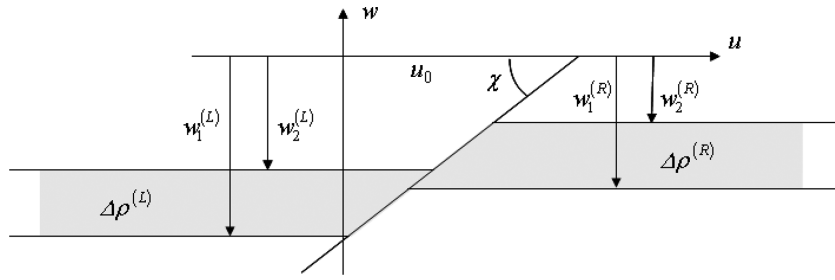


**Figure B.1.** Model of a dip-slip fault and associated parameters.

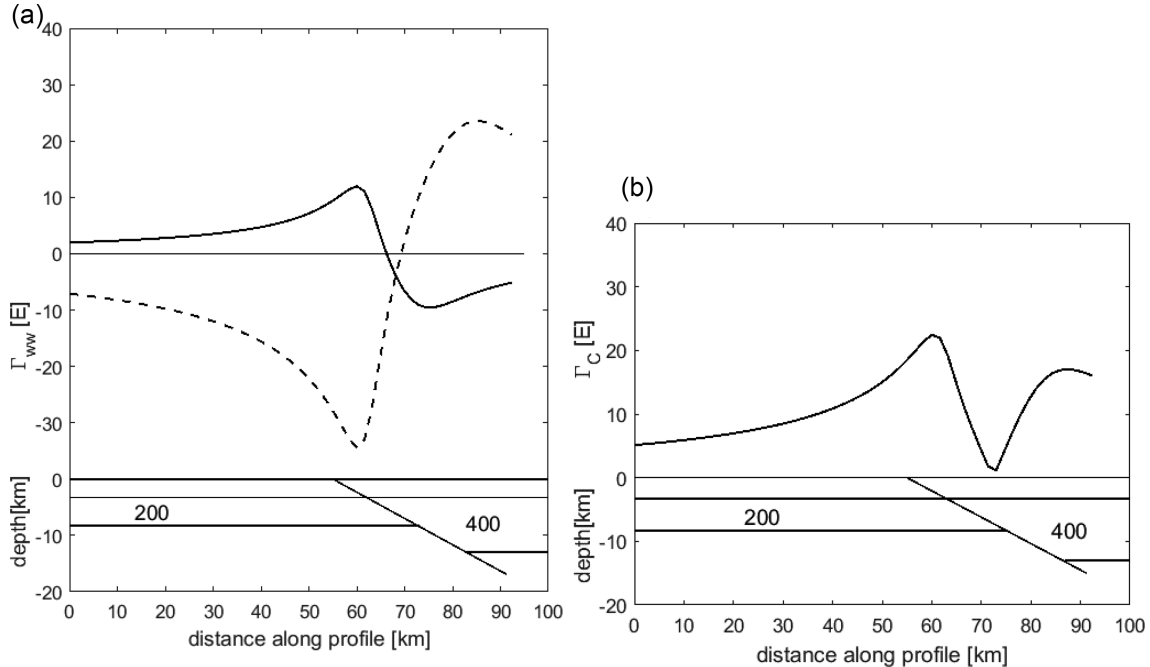


**Figure B.2.** (a) The gravitational gradients,  $\Gamma_{ww}(u, 0)$ , due to density contrasts (indicated in units of  $\text{kg m}^{-3}$ ) on either side of the fault and other parameters as indicated for Test 3.1 (Table 3). The solid line is the gradient,  $\Gamma_{ww}^{(L)}(u, 0)$ , generated by the contrast to the left of the fault; and the dashed line is the gradient,  $\Gamma_{ww}^{(R)}(u, 0)$ , generated by the contrast to the right. (b) The graph shows the resultant gravitational gradient,  $\Gamma_C = |\Gamma_{ww}| = |\Gamma_{ww}^{(L)} + \Gamma_{ww}^{(R)}|$ .

$$D^{(L,R)} = \frac{E_2^{(L,R)} \theta_2^{(L,R)} - E_1^{(L,R)} \theta_1^{(L,R)}}{E^2 \sin \chi}, \quad (\text{B4})$$

$$F_{1,2}^{(L,R)} = w - w_{1,2}^{(L,R)} + E \cos \chi, \quad (\text{B8})$$

$$\theta_{1,2}^{(L,R)} = \tan^{-1} \frac{u - u_0 - w_{1,2}^{(L,R)} \cot \chi}{w - w_{1,2}^{(L,R)}}, \quad (\text{B5})$$

$$G_{1,2}^{(L,R)} = (u - u_0 - w_{1,2}^{(L,R)} \cot \chi)^2 + (w - w_{1,2}^{(L,R)})^2. \quad (\text{B9})$$

$$E = (u - u_0) \sin \chi - w \cos \chi, \quad (\text{B6})$$

$$E_{1,2}^{(L,R)} = (u - u_0) \sin \chi - w_{1,2}^{(L,R)} \cos \chi, \quad (\text{B7})$$

Fig. B.2 shows how the gradients due to the left- and right-density contrasts of the fitted model for the Burch Fault presented in Table 3 combine to form the magnitude of the differential-curvature gradient at ground level,  $\Gamma_C(u, 0) = |\Gamma_{ww}(u, 0)|$ .